Deposition of Water Vapor on Au(001) Substrates: Effect of Temperature and Deposition Frequency

Yifan Li and Haishan Cao*

ACCESS | Metrics & More | Article Recommendations | Supporting Information

ABSTRACT: Ice formation from water vapor is a common phenomenon with significant implications for both natural ice formation and industrial processes. However, there remains controversy over how deposition frequency and substrate temperature affect the structural forms of deposition products and their formation processes. In this study, we employed molecular dynamics simulations to investigate the deposition process of water vapor onto a cold Au(001) substrate at different temperatures and deposition frequencies. We analyzed the effects of temperature and deposition frequency on the forms of deposition products including bilayer hexagonal ice, amorphous water, and their mixtures. Additionally, we identified and explained the unique formation of square ice as an unstable intermediate within specific temperature and deposition frequency ranges. We also discuss the crystallization processes of pancake- and droplet-like amorphous waters. This research contributes to a better understanding of ice formation, with implications for more accurate forecasting of natural ice formation and improved control of artificial ice processes.
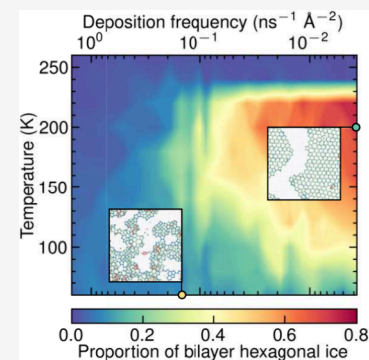
Ice formation from water vapor is a common phenomenon, encompassing various realms in nature such as astrophysical ice,[1−5] atmospheric ice,[6−9] and ice in freezing soil.[10] Vapor-to-ice conversion in celestial bodies involves the origins of comets[1−3] and the early evolution of the solar system.[4,5] Atmospheric ice research encompasses ice forms in clouds,[6] mechanisms of nucleation for various aerosols and surface sites,[7,8] and the competition between homogeneous and heterogeneous nucleation.[9] Meanwhile, vapor flow in freezing soil may lead to significant ice formation, serving as a primary mechanism for water migration.[10] Furthermore, vapor-to-ice conversion finds numerous applications in engineering. For instance, ice lithography utilizes amorphous ice formed by vapor deposition as a substitute for traditional organic polymer resists in electron beam lithography.[11−13] Binns et al.[14] devised a method where nanoparticles were codeposited with water vapor and embedded within continuously growing ice layers, subsequently melting the ice to obtain the desired suspension of nanoparticles. Additionally, in various engineering domains like heat exchangers,[15] refrigeration,[16] aircraft wings,[17] and turbine blades,[18] frost formation is to be minimized wherever possible.[19] In essence, understanding the mechanisms of vapor-to-ice conversion is paramount across multiple fields.

The experimental investigations of water vapor deposition onto cold surfaces involve various substrates, including Ru(001),[20,21] Au(001),[22] Au(111),[20,23] Pt(111),[24−27] Ir(111),[28,29] Pt(533),[30] graphene,[31] graphite,[32−34] ice,[35] CsI,[36] and borosilicate glass[6] among others. The main findings of previous experimental investigations are summarized in Supporting Table S1, and both the substrate and temperature affect the forms of deposition products. However, there is little

discussion on the effect of deposition frequency (the number of water molecules deposited onto the substrate per unit time and unit area) on the forms of deposition products. In the realm of simulations, most studies also have focused on the role of temperature and substrate, rather than deposition frequency, on the forms of the deposition products.[32,37−42] Hudait et al.[43] simulated the deposition process of water vapor on the Ih(0001) and Ic(111) substrate at deposition frequencies ranging from 1.015×10^{-3} to 5.075×10^{-2} ns^{-1} Å^{-2} and temperatures ranging from 200 to 260 K. Within ranges, only hexagonal ice was obtained. Moreover, Hudait et al.[43] predicted that higher deposition frequencies could lead to the formation of amorphous water.

Given the dearth of research on the influence of deposition frequency on water vapor deposition processes in both experiments and simulations, this study focuses on the ice formation process of water vapor on Au(001) substrates at different temperatures and deposition frequencies. Here, we have obtained the forms of deposition products within the temperature range between 60 and 260 K and the deposition frequency range between 3.758×10^{-3} and 1.503 ns^{-1} Å^{-2}. The deposition products included three forms of water, which were amorphous water, bilayer hexagonal ice (BHI, using the

terminology proposed by Ma et al.,[23,44] also named Nebraska ice[45]), and their mixtures. It was observed that within the temperature range of 60−220 K, a decrease in deposition frequency correlates with an increase in the proportion of bilayer hexagonal ice generated at a given temperature. Meanwhile, it was discovered that an unstable intermediate product—square ice appears within specific temperature and deposition frequency ranges. Furthermore, we investigated the influence of temperature on the crystallization process of amorphous water.

In the simulations of water vapor deposition onto Au(001) substrates, 1000 water molecules were deposited sequentially within the temperature range between 60 and 260 K and deposition frequency range between 3.758×10^{-3} and 1.503 $ns^{-1} Å^{-2}$. Due to the substrate effect, it is difficult to distinguish whether the deposited products adsorbed on the substrate surface are supercooled water or glassy water, we here collectively refer to the two phases of water as amorphous water. Amorphous water, as a metastable phase, will transform into crystalline ice, but its crystallization time is larger than the simulation time. The deposition products of 1000 water molecules within the given temperature and deposition frequency range may consist of BHI, amorphous water, or a mixture of both. We used the polyhedral template matching (PTM) algorithm[46] to analyze the ratio of BHI formed at different temperatures and deposition frequencies, with the root-mean-square deviation (RMSD) cutoff set to 0.2 (see Figure 1). Since the monolayer structure of BHI closely resembles that of graphene after scaling normalization, a water molecule was identify as part of the BHI structure if its RMSD value compared to graphene was below 0.2.

Figure 1a shows the BHI proportion of deposition products with 1000 water molecules at various temperatures and deposition frequencies. The deposition products could be categorized visually based on the BHI proportion, from high to low, into BHI (BHI proportion ⩾ 40%), a mixture of BHI and amorphous water (10% ⩽ BHI proportion < 40%), and amorphous water (BHI proportion < 10%). Amorphous water could further be divided into two types: droplet- and pancake-like amorphous water. Droplet-like amorphous water only appeared at temperatures equal to or higher than 240 K. This is because water molecules initially form pancake-like amorphous water upon deposition, as the probability distribution of deposition positions is uniform in the xy-plane of the simulation domain. At temperatures below 240 K, even if droplet-like amorphous water is more thermodynamically stable than the pancake-like form, the slow diffusion of water molecules prevents the transition to droplet-like amorphous water before the simulation ends. At temperatures equal to or higher than 240 K, the faster diffusion of water molecules allows pancake-like amorphous water to transition into the droplet-like form, with the transition process at 240 K shown in Supporting Video S2. At temperatures ranging from 240 to 260 K, only amorphous water was formed. At temperatures equal to and below 220 K, predominantly BHI was formed when the deposition frequency was lower than $1 \times 10^{-2} ns^{-1} Å^{-2}$. With a deposition frequency slightly higher than $1 \times 10^{-2} ns^{-1} Å^{-2}$, a coexistence of BHI with amorphous water could occur. However, when the deposition frequency exceeded 0.4 $ns^{-1} Å^{-2}$, only amorphous water was generated. In general, higher deposition frequencies tended to favor the formation of amorphous water, while lower frequencies favored the formation of BHI at a given temperature. This corresponds
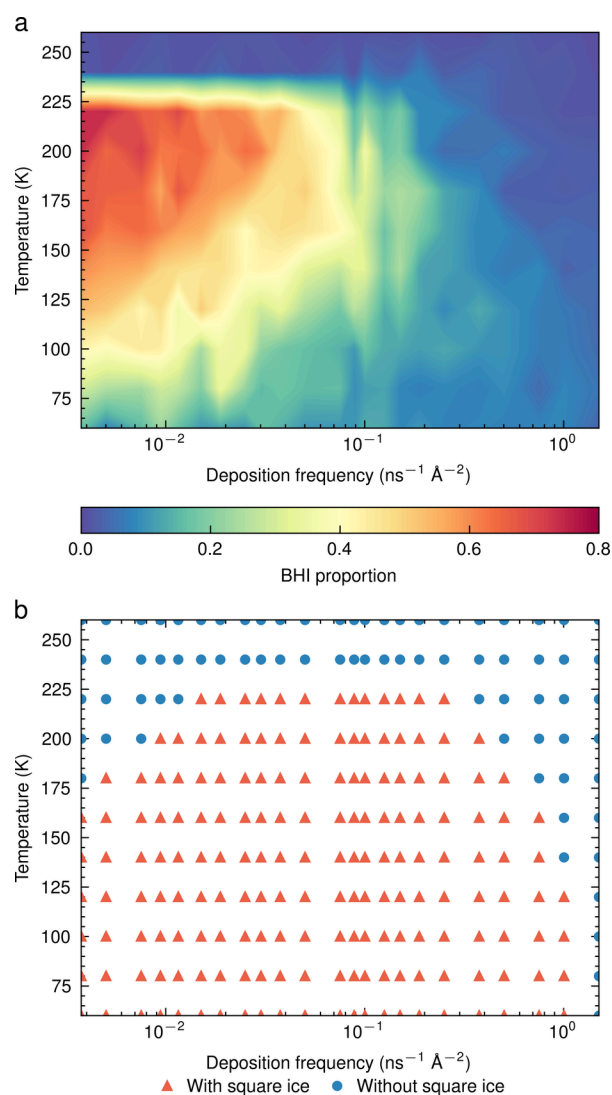

Figure 1. Deposition products at different temperatures and deposition frequencies. (a) BHI proportion of the deposition products after depositing 1000 water molecules at varying temperatures and deposition frequencies. It should be noted that, due to the principles of the PTM algorithm, water molecules at the edges of BHI clusters do not have enough neighboring water molecules and thus are not included in the recognition of BHI. Therefore, the obtained BHI proportion can be underestimated compared to the actual value. (b) Temperature and deposition frequency ranges for the appearance (red triangles) and absence (blue circles) of square ice during the simulation process.

to the experimental observation that excessively high deposition frequencies disrupt the formation process of crystal structures in newly deposited water molecules.[47] Meanwhile, lower temperatures corresponded to a wider range of deposition frequencies where amorphous water formation occurred at temperatures below 180 K. Moreover, a lower deposition frequency led to a higher BHI proportion at temperatures ranging from 60 to 240 K, which is consistent with the conclusion drawn by Watanabe and Kouchi.[48] It is worth pointing out that square ice, similar to the ice structure reported by Algara-Siller et al.,[49] could appear within the temperature and deposition frequency ranges indicated by the red triangles shown in Figure 1b. Square ice, as an unstable intermediate product, could only exist on the order of
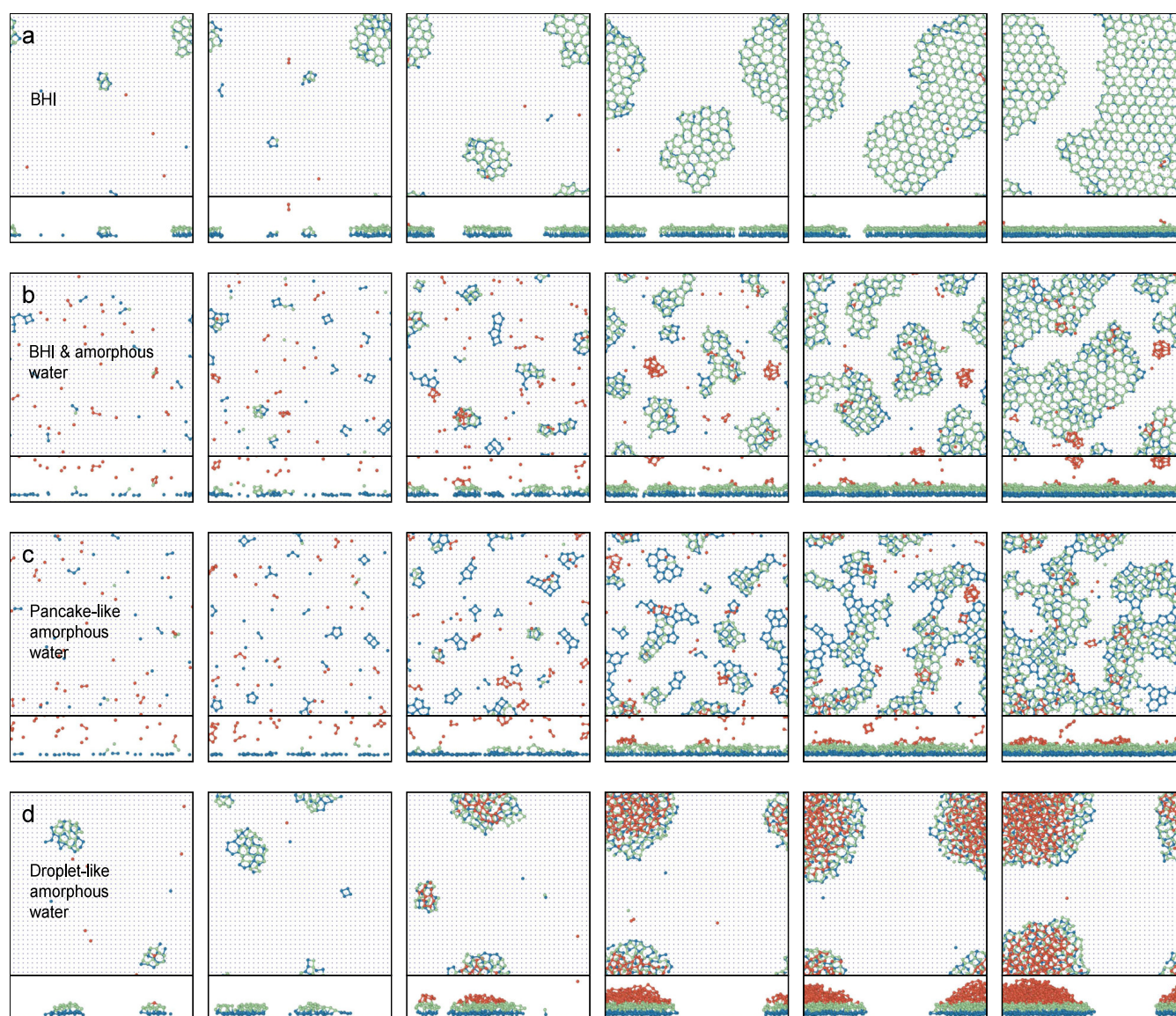
Figure 2. Snapshots of the deposition processes for products with different BHI proportions, with the top and bottom panels showing top and front views of the system, respectively. (a) BHI (at 200 K, 3.758×10^{-3} ns^{-1} Å^{-2}, 73.7% BHI). (b) BHI & amorphous water (at 140 K, 1.503×10^{-1} ns^{-1} Å^{-2}, 24.6% BHI). (c) pancake-like amorphous water (at 60 K, 1.503×10^{-1} ns^{-1} Å^{-2}, 8.4% BHI). (d) droplet-like amorphous water (at 260 K, 3.758×10^{-3} ns^{-1} Å^{-2}, 1.2% BHI). Each row sequentially shows the system after depositing 75, 125, 250, 500, 750, and 1000 water molecules, from left to right. The first layer of water molecules on the substrate is shown in blue, the second layer in green, and the remaining water molecules in red. The Au atoms are shown in light blue.

nanoseconds or even shorter within these temperature and deposition frequency ranges, shorter than the total simulation time. Since the mW model is a coarse-grained model that cannot represent proton ordering, the influence of the hydrogen bond patterns was not considered here.

Deposition dynamics of water vapor on Au(001) substrates are discussed below. Four typical deposition processes of BHI, amorphous water, and a mixture of both are shown in Figure 2. Collectively, multiple clusters generally formed first during the deposition process. These clusters continuously grew and merged, eventually forming one large cluster. Apart from the formation of droplet-like amorphous water clusters, bilayer water clusters were more stable than monolayer and multilayer water clusters. The formation process of BHI clusters during the deposition process involved following steps: the deposited water molecules first formed small monolayer water clusters,

which then transformed into bilayer water clusters. The detailed process can be seen in Supporting Video S1. After the formation of the small bilayer water clusters, the subsequent growth law is shown in Figure 2a. Small clusters continuously grew and merged, transforming into BHI clusters, and zigzag and armchair edge structures appeared. This coincides with the experimental observations and simulation results of Ma et al.[23] In the early stages of the deposition process corresponding to Figure 2b,c, small monolayer clusters of tetramers, pentamers, and a few hexamers were initially formed. These clusters then continued to grow into BHI or square ice which will be discussed in the next section. Newly inserted water molecules would deposit in different regions: some deposited in areas away from other clusters, forming new clusters; some deposited at the edges of existing clusters and were adsorbed by them, causing the clusters to grow in the *xy*-direction; some
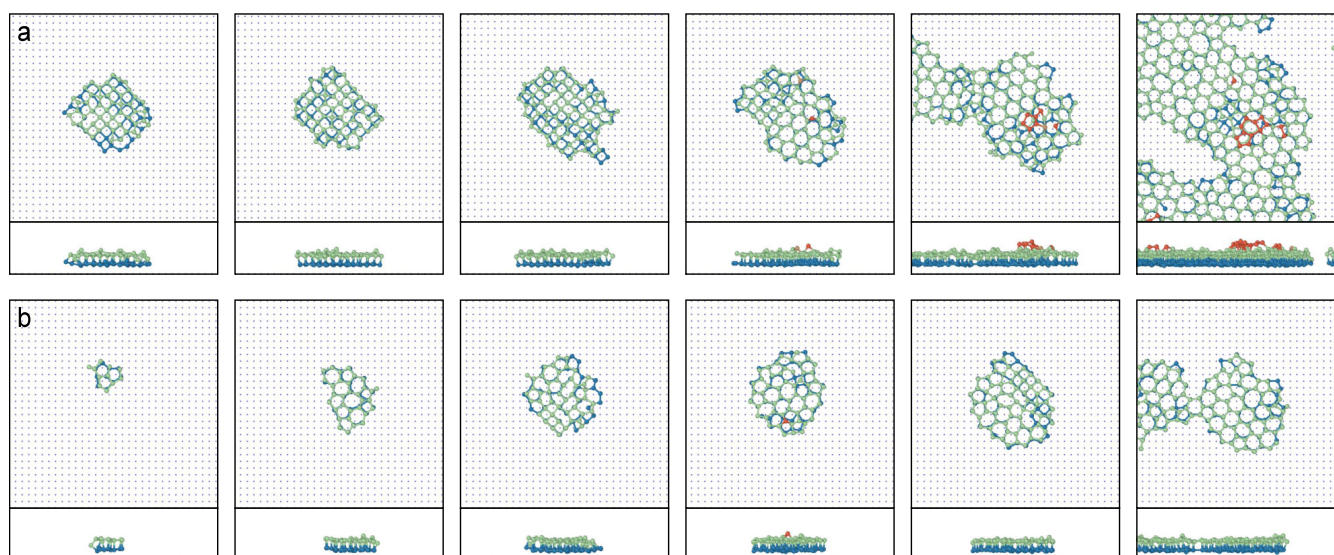
Figure 3. Transformation process of square ice. (a) Snapshots of the growth process of square ice clusters (at 140 K, 1.879×10^{-2} ns^{-1} Å^{-2}) after depositing 375, 450, 525, 600, 800, and 1000 water molecules, from left to right. (b) Snapshots of the process where part of the BHI transforms into square ice and eventually transforms back into BHI (at 180 K, 1.879×10^{-2} ns^{-1} Å^{-2}) after depositing 180, 220, 340, 380, 480, and 510 water molecules, from left to right. To highlight key features, most water molecules outside the square ice have been hidden. The remaining settings are the same as described in Figure 2.

water molecules deposited on the first layer of water molecules, becoming the second layer; and some water molecules deposited on the second layer, attracted by nearby third-layer water molecules, or they did not have enough time to diffuse to the cluster edges before the deposition ended to let the trilayer water clusters to transform into bilayer water clusters, resulting in the presence of third-layer water molecules in the final deposition product. When the deposition frequency exceeded approximately 1×10^{-2} ns^{-1} Å^{-2}, the newly inserted water molecules would disrupt the relaxation process of the existing water molecules toward their corresponding lattice sites, leading to the formation of amorphous water. Pancake-like amorphous water transformed into BHI over time, and the crystallization time decreased with increasing temperature. Since the deposition frequencies for Figure 2b,c are the same, the crystallization time scale at 140 K (2b) was closer to the deposition time scale, resulting in a partial transformation of amorphous water into BHI. In contrast, at 60 K (2c), the crystallization time for amorphous water was much longer than the deposition time scale, resulting in almost all amorphous water at the end of deposition. In the front view, a small number of water molecules appeared to be suspended in midair because the higher deposition frequencies in these cases led to shorter total deposition times, and these water molecules did not have enough time to be adsorbed by the substrate or the clusters on the substrate before the deposition ended. In the deposition process corresponding to Figure 2d, multiple small water clusters first formed. These clusters continuously grew and merged, eventually combining into a single droplet-like amorphous water cluster. The detailed process can be seen in Supporting Video S2.

Square ice, as an unstable intermediate product, could transform into a stable state in two typical pathways shown in Figure 3. First, square ice clusters could continually grow until they become large enough to transform into BHI, or they could attract and merge with other clusters before transitioning into BHI (see Figure 3a). Additionally, BHI structures could

also transform into square ice (see Figure 3b). However, square ice is only a metastable product with higher potential energy than BHI, and it would eventually transform into BHI once it grows to a certain size. More discussions on potential energy of square ice and BHI can be found in the Supporting Information.

To investigate the influence of the substrate on the formation of square ice, we simulated the deposition process on substrates with different crystal planes, lattice constants, and hydrophilic properties at temperatures of 140 and 180 K and a deposition frequency of 1.879×10^{-2} ns^{-1} Å^{-2}, corresponding to the cases in Figure 3. Our findings show that square ice did not form on the Au(111) substrate. By varying the substrate's lattice constant from 4.078 Å to values between 3.9 and 4.2 Å in 0.1 Å increments, we observed that square ice did not form at 3.9 Å, but appeared at 4.0−4.2 Å, becoming most stable and forming large clusters at 4.2 Å. However, at 4.0 Å, square ice was short-lived. We believe this behavior is due to lattice matching between the substrate and square ice, where the substrate's lattice constant influences that of square ice. In the simulations, the observed spacing between water molecules within the same layer of square ice is approximately $\frac{\sqrt{2}}{2} a_{sub}$, where a_{sub} is the substrate's lattice constant. The square ice structure is more stable when $a_{sub} = 4.2$ Å compared to other values. By varying the energy parameter (ε) of the gold-water Lennard-Jones potential from 1.553 kJ/mol to values between 1.1 and 1.7 kJ/mol in 0.1 kJ/mol increments, we observed that square ice did not form at 1.1 or 1.2 kJ/mol, but appeared at 1.3−1.7 kJ/mol, with the longest lifetime observed at 1.7 kJ/mol. This is because hydrophobic substrates are more likely to promote the formation of droplet-like amorphous water rather than bilayer crystalline ice. In contrast, on hydrophilic substrates, water molecules are strongly adsorbed onto the substrate surface, restricting their diffusion to other positions and thus stabilizing the structure. The influence of substrates on the form of deposition products aligns with the findings of
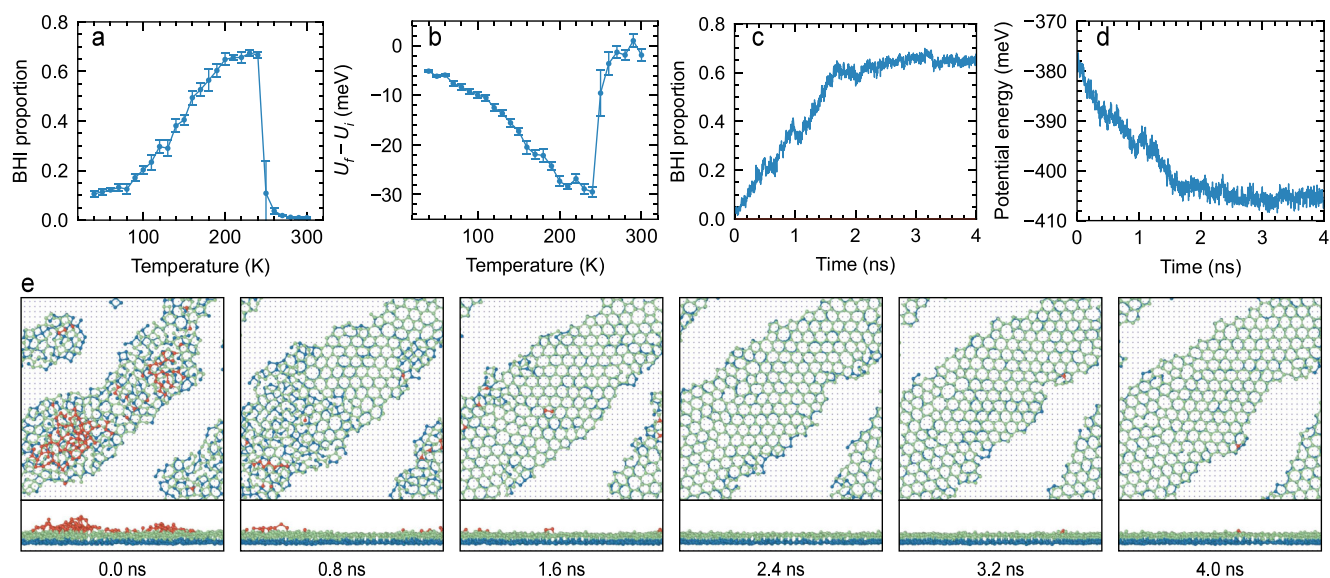
Figure 4. Phase transition process of pancake-like amorphous water. (a) BHI proportion and (b) change in potential energy per water molecule after 4 ns at different temperatures. U_i and U_f refer to the potential energy per water molecule at initial and final moments of the phase transition process at a given temperature, respectively. (c) BHI proportion and (d) potential energy per water molecule versus time for the phase transition process at 240 K. (e) Snapshots of the phase transition process at 240 K. The potential energy considered both the potential energy between water molecules and the substrate and the potential energy among the water molecules themselves. The error bars in (a) and (b) represent the 95% confidence interval.
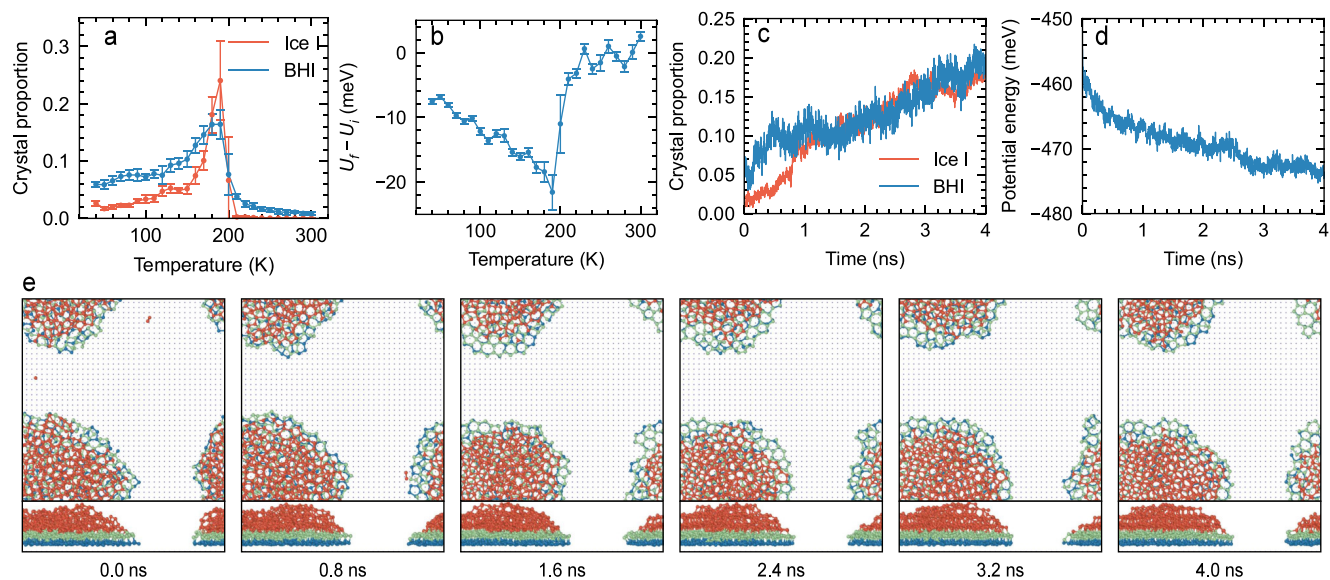
Figure 5. Phase transition process of droplet-like amorphous water. (a) Crystal proportion and (b) change in potential energy per water molecule after 4 ns at different temperatures. U_i and U_f refer to the potential energy per water molecule at initial and final moments of the phase transition process at a given temperature, respectively. (c) Crystal proportion and (d) potential energy per water molecule versus time for the phase transition process at 180 K. (e) Snapshots of the phase transition process at 180 K. The potential energy considered both the potential energy between water molecules and the substrate and the potential energy among the water molecules themselves. The error bars in (a) and (b) represent the 95% confidence interval.

Lupi et al.,[39] which also highlights the impact of substrates on deposition products.

Since the mW model lacks proton information, we employed the TIP4P/Ice model[50] for simulation to validate the stability of the square ice. At temperatures of 140 and 180 K and a deposition frequency of 1.879×10^{-2} ns^{-1} Å^{-2}, only amorphous water clusters formed. Considering the slower crystallization dynamics of the TIP4P model compared to the mW model,[51] we hypothesize that reducing the deposition

frequency could provide water molecules with more time to crystallize. Further simulations with lower deposition frequencies supported this hypothesis. At temperatures of 140 and 180 K, and a deposition frequency of 1.879×10^{-3} ns^{-1} Å^{-2}, a certain amount of square ice was observed (see Figure S7). At a temperature of 180 K and a deposition frequency of 7.517×10^{-4} ns^{-1} Å^{-2}, droplet-like amorphous water clusters with small amounts of BHI at the edges were observed—about 9.8% at the end of the simulation (see Figure S8a). As the

temperature decreased from 180 to 140 K, the diffusion was reduced, resulting in a smaller amount of BHI—about 4.0% at the end of the simulation (see Figure S8b).

To investigate the effect of temperature on the crystallization process of amorphous water, we used pancake-like amorphous water obtained at a deposition frequency of 0.1503 ns^{-1} Å^{-2} and a temperature of 240 K (retaining only the water molecules adsorbed on Au(001) substrate to exclude the influence of water clusters suspended in the midair) and droplet-like amorphous water obtained at a deposition frequency of 3.758×10^{-3} ns^{-1} Å^{-2} and a temperature of 240 K as initial configurations. The two configurations were cooled or heated to target temperatures ranging from 40 to 300 K within 0.02 ns and then simulated for 4 ns to investigate phase transition processes.

For pancake-like amorphous water, no crystallization was observed within 4 ns at temperatures greater than or equal to 260 K, which is reflected by almost zero BHI proportion shown in Figure 4a and minor change in potential energy shown in Figure 4b. At temperatures less than or equal to 250 K, the crystallization process was observed, where the pancake-like amorphous water began to transform into BHI. The lower the temperature, the slower the crystallization of the pancake-like amorphous water due to the slower diffusion of water molecules at lower temperatures. The error bar for the BHI proportion at 250 K is relatively large because the crystallization time of pancake-like amorphous water at 250 K is close to the simulation time of 4 ns, causing some cases to crystallize while others do not. The melting temperature of BHI under the current simulation conditions was determined to be approximately 264.6 K, with detailed methods described in the Supporting Information. The pancake-like amorphous water did not transform into BHI at 260 K because the crystallization time at this temperature exceeds the total simulation time of 4 ns. Figure 4c,d shows how the BHI proportion and change in potential evolved with time for the phase transition process of pancake-like amorphous water at 240 K described in Figure 4e. The BHI proportion exhibited a rapid increase between 0 and 1.6 ns, accompanied by the corresponding change in potential energy per water molecule, which elucidates the transition of amorphous water to the more stable BHI form.

For droplet-like amorphous water, no significant crystallization was observed within the 4 ns simulation time at temperatures greater than 200 K and less than or equal to 150 K as shown in Figure 5a,b. At temperatures between 160 and 200 K, the droplet-like amorphous water partially transformed into ice I and BHI within 4 ns. The error bars for the crystal proportion at 190 and 200 K are relatively large because the crystallization times of droplet-like amorphous water at these temperatures are close to the simulation time of 4 ns, causing some cases to crystallize while others do not. At temperatures less than or equal to 190 K, the lower the temperature, the slower the kinetics of crystallization, resulting in a smaller change in the potential energy. At temperatures greater than or equal to 190 K, the free energy barrier for the nucleation of water rises with increasing temperature, reducing the thermodynamic driving force for crystallization.[52] Figure 5c,d shows how the crystal proportion and change in potential evolved with time for the phase transition process of droplet-like amorphous water at 180 K described in Figure 5e.

Figures 4 and 5 show that the temperature with the highest proportion of crystalline ice is 240 K for pancake-like amorphous water and 190 K for droplet-like amorphous water. This difference can be analyzed from both kinetic and thermodynamic perspectives, using concepts from classical nucleation theory. Kinetically, pancake-like amorphous water has a larger contact area with the substrate, and the substrate mainly interacts with the first two layers of water molecules, resulting in stronger interactions with pancake-like amorphous water compared to droplet-like amorphous water. This leads to a smaller self-diffusion coefficient for pancake-like amorphous water. Thermodynamically, however, pancake-like amorphous water has a structure closer to Ice I and BHI, with a lower free energy barrier for nucleation. As a result, the crystallization of pancake-like amorphous water can be observed within 4 ns at temperatures between 200 and 240 K. In contrast, droplet-like amorphous water has a higher free energy barrier, making crystallization more challenging.

In summary, we investigated the deposition process of water molecules onto a cold Au(001) substrate at varying temperatures and deposition frequencies using molecular dynamics simulations. Unlike previous studies that mainly focused on the influence of temperature or substrate material on deposition products, this study confirmed the effect of deposition frequency on the form of deposition products. The observed forms of deposition products included BHI, amorphous water, and their mixtures within the range of temperatures from 60 to 260 K and deposition frequencies from 3.758×10^{-3} to 1.503 ns^{-1} Å^{-2}. Square ice, an unstable intermediate product, was observed briefly during the deposition process within specific temperature and deposition frequency ranges. Moreover, the crystallization processes of pancake- and droplet-like amorphous waters were investigated, and the maximum degree of crystallization in 4 ns was found at 240 K for pancake-like amorphous water and 190 K for droplet-like amorphous water. These findings provide valuable insights into the understanding of the deposition mechanisms of water vapor on cold substrates and the crystallization dynamics of amorphous water.

■ METHODS

We conducted deposition simulations of water vapor on an Au(001) substrate using LAMMPS,[53] employing the monatomic water (mW) model for water–water interactions[54] and the 12-6 Lennard-Jones potential to describe interactions between water molecules and Au atoms. To validate the simulation model's accuracy, we computed the radial distribution function and contact angle of liquid water, confirming that the model effectively reproduces both the water structure and the interaction strength between water molecules and gold atoms. Additional details on the simulation settings and model validation are provided in the Supporting Information.

■ ASSOCIATED CONTENT

ⓢ Supporting Information

The Supporting Information is available free of charge at https://pubs.acs.org/doi/10.1021/acs.jpclett.4c02705.

> Video S1: The early stages of the formation process of BHI clusters during the deposition process, i.e., the process of forming small bilayer water clusters (MP4)

> Video S2: The formation process of droplet-like amorphous water clusters during the deposition process (MP4)

Summary of experimental investigations of water vapor deposition on cold substrates, simulation settings, model validation, square ice analysis, and the melting temperature of BHI (PDF)

■ AUTHOR INFORMATION

Corresponding Author

Haishan Cao − *Key Laboratory for Thermal Science and Power Engineering of Ministry of Education, Department of Energy and Power Engineering, Tsinghua University, Beijing 100084, People's Republic of China;* orcid.org/0000-0003-1621-8592; Email: HaishanCao@tsinghua.edu.cn

Author

Yifan Li − *Key Laboratory for Thermal Science and Power Engineering of Ministry of Education, Department of Energy and Power Engineering, Tsinghua University, Beijing 100084, People's Republic of China;* orcid.org/0009-0009-9765-8696

Complete contact information is available at:
https://pubs.acs.org/10.1021/acs.jpclett.4c02705

Notes

The authors declare no competing financial interest.

■ REFERENCES

(1) Davies, J. K.; Roush, T. L.; Cruikshank, D. P.; Bartholomew, M. J.; Geballe, T. R.; Owen, T.; de Bergh, C. The detection of water ice in comet Hale-Bopp. *Icarus* **1997**, *127*, 238−245.

(2) Sunshine, J. M.; A'Hearn, M. F.; Groussin, O.; Li, J.-Y.; Belton, M. J. S.; Delamere, W. A.; Kissel, J.; Klaasen, K. P.; McFadden, L. A.; Meech, K. J.; et al. Exposed Water Ice Deposits on the Surface of Comet 9P/Tempel 1. *Science* **2006**, *311*, 1453−1455.

(3) Filacchione, G.; De Sanctis, M. C.; Capaccioni, F.; Raponi, A.; Tosi, F.; Ciarniello, M.; Cerroni, P.; Piccioni, G.; Capria, M. T.; Palomba, E.; et al. Exposed water ice on the nucleus of comet 67P/Churyumov−Gerasimenko. *Nature* **2016**, *529*, 368−372.

(4) Kouchi, A. Vapour pressure of amorphous H2O ice and its astrophysical implications. *Nature* **1987**, *330*, 550−552.

(5) Kouchi, A.; Yamamoto, T. Cosmoglaciology: Evolution of ice in interstellar space and the early solar system. *Progress in crystal growth and characterization of materials* **1995**, *30*, 83−107.

(6) Mangan, T. P.; Plane, J. M. C.; Murray, B. J. The Phase of Water Ice Which Forms in Cold Clouds in the Mesospheres of Mars, Venus, and Earth. *Journal of Geophysical Research: Planets* **2021**, *126*, No. e2020JE006796.

(7) Zobrist, B.; Marcolli, C.; Pedernera, D. A.; Koop, T. Do atmospheric aerosols form glasses? *Atmos. Chem. Phys.* **2008**, *8*, 5221−5244.

(8) Freedman, M. A. Potential Sites for Ice Nucleation on Aluminosilicate Clay Minerals and Related Materials. *J. Phys. Chem. Lett.* **2015**, *6*, 3850−3858.

(9) Murray, B. J.; Jensen, E. J. Homogeneous nucleation of amorphous solid water particles in the upper mesosphere. *Journal of Atmospheric and Solar-Terrestrial Physics* **2010**, *72*, 51−61.

(10) Zhang, S.; Teng, J.; He, Z.; Sheng, D. Importance of vapor flow in unsaturated freezing soil: a numerical study. *Cold Regions Science and Technology* **2016**, *126*, 1−9.

(11) King, G. M.; Schürmann, G.; Branton, D.; Golovchenko, J. A. Nanometer Patterning with Ice. *Nano Lett.* **2005**, *5*, 1157−1160.

(12) Hong, Y.; Zhao, D.; Liu, D.; Ma, B.; Yao, G.; Li, Q.; Han, A.; Qiu, M. Three-Dimensional in Situ Electron-Beam Lithography Using Water Ice. *Nano Lett.* **2018**, *18*, 5036−5041.

(13) Haque, R. I.; Waafi, A. K.; Jaemin, K.; Briand, D.; Han, A. 80 K cryogenic stage for ice lithography. *Micro and Nano Engineering* **2022**, *14*, 100101.

(14) Binns, C.; Prieto, P.; Baker, S.; Howes, P.; Dondi, R.; Burley, G.; Lari, L.; Kroger, R.; Pratt, A.; Aktas, S.; Mellon, J. K. Preparation of hydrosol suspensions of elemental and core−shell nanoparticles by co-deposition with water vapour from the gas-phase in ultra-high vacuum conditions. *J. Nanopart. Res.* **2012**, *14*, 1136.

(15) Li, Z.; Wei, W.; Wang, W.; Sun, Y.; Wang, S.; Lin, Y.; Huang, C.; Deng, S. Experimental study on the effects of melted frost icing on the operating performances of air source heat pump. *Applied Thermal Engineering* **2024**, *238*, 122136.

(16) Wang, F.; Liang, C.; Zhang, X. Research of anti-frosting technology in refrigeration and air conditioning fields: A review. *Renewable and Sustainable Energy Reviews* **2018**, *81*, 707−722.

(17) Koszut, J.; Boyina, K.; Popovic, G.; Carpenter, J.; Wang, S.; Miljkovic, N. Superhydrophobic heat exchangers delay frost formation and reduce defrost energy input of aircraft environmental control systems. *Int. J. Heat Mass Transfer* **2022**, *189*, 122669.

(18) Fakorede, O.; Feger, Z.; Ibrahim, H.; Ilinca, A.; Perron, J.; Masson, C. Ice protection systems for wind turbines in cold climate: characteristics, comparisons and analysis. *Renewable and Sustainable Energy Reviews* **2016**, *65*, 662−675.

(19) Walker, C.; Lerch, S.; Reininger, M.; Eghlidi, H.; Milionis, A.; Schutzius, T. M.; Poulikakos, D. Desublimation Frosting on Nanoengineered Surfaces. *ACS Nano* **2018**, *12*, 8288−8296.

(20) Smith, R. S.; Huang, C.; Wong, E. K. L.; Kay, B. D. Desorption and crystallization kinetics in nanoscale thin films of amorphous water ice. *Surf. Sci.* **1996**, *367*, L13−L18.

(21) Yamauchi, T.; Mine, K.; Nakashima, Y.; Izumi, A.; Namiki, A. Crystallization of D2O thin films on Ru(0 0 1) surfaces. *Appl. Surf. Sci.* **2009**, *256*, 1124−1127.

(22) Yang, P.; Zhang, C.; Sun, W.; Dong, J.; Cao, D.; Guo, J.; Jiang, Y. Robustness of Bilayer Hexagonal Ice against Surface Symmetry and Corrugation. *Phys. Rev. Lett.* **2022**, *129*, 046001.

(23) Ma, R.; Cao, D.; Zhu, C.; Tian, Y.; Peng, J.; Guo, J.; Chen, J.; Li, X.-Z.; Francisco, J. S.; Zeng, X. C.; et al. Atomic imaging of the edge structure and growth of a two-dimensional hexagonal ice. *Nature* **2020**, *577*, 60−63.

(24) Stevenson, K. P.; Kimmel, G. A.; Dohnálek, Z.; Smith, R. S.; Kay, B. D. Controlling the Morphology of Amorphous Solid Water. *Science* **1999**, *283*, 1505−1507.

(25) Dohnálek, Z.; Kimmel, G. A.; Ciolli, R. L.; Stevenson, K. P.; Smith, R. S.; Kay, B. D. The effect of the underlying substrate on the crystallization kinetics of dense amorphous solid water films. *J. Chem. Phys.* **2000**, *112*, 5932−5941.

(26) Kimmel, G. A.; Stevenson, K. P.; Dohnálek, Z.; Smith, R. S.; Kay, B. D. Control of amorphous solid water morphology using molecular beams. I. Experimental results. *J. Chem. Phys.* **2001**, *114*, 5284−5294.

(27) Thürmer, K.; Nie, S. Formation of hexagonal and cubic ice during low-temperature growth. *Proc. Natl. Acad. Sci. U. S. A.* **2013**, *110*, 11757−11762.

(28) Harada, K.; Sugimoto, T.; Kato, F.; Watanabe, K.; Matsumoto, Y. Thickness dependent homogeneous crystallization of ultrathin amorphous solid water films. *Phys. Chem. Chem. Phys.* **2020**, *22*, 1963−1973.

(29) Safarik, D. J.; Mullins, C. B. The nucleation rate of crystalline ice in amorphous solid water. *J. Chem. Phys.* **2004**, *121*, 6003−6010.

(30) Backus, E. H. G.; Grecea, M. L.; Kleyn, A. W.; Bonn, M. Surface Crystallization of Amorphous Solid Water. *Phys. Rev. Lett.* **2004**, *92*, 236101.

(31) Kimmel, G. A.; Matthiesen, J.; Baer, M.; Mundy, C. J.; Petrik, N. G.; Smith, R. S.; Dohnálek, Z.; Kay, B. D. No Confinement Needed: Observation of a Metastable Hydrophobic Wetting Two-Layer Ice on Graphene. *J. Am. Chem. Soc.* **2009**, *131*, 12838−12844.

(32) Andersson, P. U.; Suter, M. T.; Marković, N.; Pettersson, J. B. C. Water Condensation on Graphite Studied by Elastic Helium Scattering and Molecular Dynamics Simulations. *J. Phys. Chem. C* **2007**, *111*, 15258−15266.

(33) Kong, X.; Andersson, P. U.; Markovic, N.; Pettersson, J. B. Environmental molecular beam studies of ice surface processes. *12th International Conference on the Physics and Chemistry of Ice (PCI-2010)* **2010**, 79−88.

(34) Zhang, X.; Xu, J.-Y.; Tu, Y.-B.; Sun, K.; Tao, M.-L.; Xiong, Z.-H.; Wu, K.-H.; Wang, J.-Z.; Xue, Q.-K.; Meng, S. Hexagonal Monolayer Ice without Shared Edges. *Phys. Rev. Lett.* **2018**, *121*, 256001.

(35) Kong, X.; Papagiannakopoulos, P.; Thomson, E. S.; Marković, N.; Pettersson, J. B. C. Water Accommodation and Desorption Kinetics on Ice. *J. Phys. Chem. A* **2014**, *118*, 3973−3979.

(36) Mitchell, E. H.; Raut, U.; Teolis, B. D.; Baragiola, R. A. Porosity effects on crystallization kinetics of amorphous solid water: Implications for cold icy objects in the outer solar system. *Icarus* **2017**, *285*, 291−299.

(37) Essmann, U.; Geiger, A. Molecular dynamics simulation of vapor deposited amorphous ice. *J. Chem. Phys.* **1995**, *103*, 4678−4692.

(38) Guillot, B.; Guissani, Y. Investigation of vapor-deposited amorphous ice and irradiated ice by molecular dynamics simulation. *J. Chem. Phys.* **2004**, *120*, 4366−4382.

(39) Lupi, L.; Kastelowitz, N.; Molinero, V. Vapor deposition of water on graphitic surfaces: Formation of amorphous ice, bilayer ice, ice I, and liquid water. *J. Chem. Phys.* **2014**, *141*, 18C508.

(40) Fitzner, M.; Pedevilla, P.; Michaelides, A. Predicting heterogeneous ice nucleation with a data-driven approach. *Nat. Commun.* **2020**, *11*, 4777.

(41) Bi, Y.; Cao, B.; Li, T. Enhanced heterogeneous ice nucleation by special surface geometry. *Nat. Commun.* **2017**, *8*, 15372.

(42) Lata, N. N.; Zhou, J.; Hamilton, P.; Larsen, M.; Sarupria, S.; Cantrell, W. Multivalent Surface Cations Enhance Heterogeneous Freezing of Water on Muscovite Mica. *J. Phys. Chem. Lett.* **2020**, *11*, 8682−8689.

(43) Hudait, A.; Molinero, V. What Determines the Ice Polymorph in Clouds? *J. Am. Chem. Soc.* **2016**, *138*, 8958−8967.

(44) Jiang, J.; Lai, Y.; Sheng, D.; Tang, G.; Zhang, M.; Niu, D.; Yu, F. Two-dimensional bilayer ice in coexistence with three-dimensional ice without confinement. *Nat. Commun.* **2024**, *15*, 5762.

(45) Bai, J.; Zeng, X. C.; Koga, K.; Tanaka, H. Formation of Quasi Two-dimensional Bilayer Ice in Hydrophobic Slits: A Possible Candidate for Ice XIII? *Mol. Simul.* **2003**, *29*, 619−626.

(46) Larsen, P. M.; Schmidt, S.; Schiøtz, J. Robust structural identification via polyhedral template matching. *Modell. Simul. Mater. Sci. Eng.* **2016**, *24*, 055007.

(47) Kouchi, A.; Yamamoto, T.; Kozasa, T.; Kuroda, T.; Greenberg, J. Conditions for condensation and preservation of amorphous ice and crystallinity of astrophysical ices. *Astron. Astrophys.* **1994**, *290*, 1009−1018.

(48) Watanabe, N.; Kouchi, A. Ice surface reactions: A key to chemical evolution in space. *Prog. Surf. Sci.* **2008**, *83*, 439−489.

(49) Algara-Siller, G.; Lehtinen, O.; Wang, F. C.; Nair, R. R.; Kaiser, U.; Wu, H. A.; Geim, A. K.; Grigorieva, I. V. Square ice in graphene nanocapillaries. *Nature* **2015**, *519*, 443−445.

(50) Abascal, J. L. F.; Sanz, E.; García Fernández, R.; Vega, C. A potential model for the study of ices and amorphous water: TIP4P/Ice. *J. Chem. Phys.* **2005**, *122*, 234511.

(51) Fitzner, M.; Sosso, G. C.; Cox, S. J.; Michaelides, A. The Many Faces of Heterogeneous Ice Nucleation: Interplay Between Surface Morphology and Hydrophobicity. *J. Am. Chem. Soc.* **2015**, *137*, 13658−13669.

(52) Sosso, G. C.; Chen, J.; Cox, S. J.; Fitzner, M.; Pedevilla, P.; Zen, A.; Michaelides, A. Crystal Nucleation in Liquids: Open Questions and Future Challenges in Molecular Dynamics Simulations. *Chem. Rev.* **2016**, *116*, 7078−7116.

(53) Thompson, A. P.; Aktulga, H. M.; Berger, R.; Bolintineanu, D. S.; Brown, W. M.; Crozier, P. S.; in 't Veld, P. J.; Kohlmeyer, A.; Moore, S. G.; Nguyen, T. D.; Shan, R.; Stevens, M. J.; Tranchida, J.; Trott, C.; Plimpton, S. J. LAMMPS - a flexible simulation tool for particle-based materials modeling at the atomic, meso, and continuum scales. *Comput. Phys. Commun.* **2022**, *271*, 108171.

(54) Molinero, V.; Moore, E. B. Water Modeled As an Intermediate Element between Carbon and Silicon. *J. Phys. Chem. B* **2009**, *113*, 4008−4016.